Journal of Molecular Modeling (2025) 31:75
https://doi.org/10.1007/s00894-025-06296-w

ORIGINAL PAPER

Structures, bonding aspects and spectroscopic parameters of morin, myricetin, and quercetin with copper/zinc complexes: DFT and TDDFT exploration

Mukhtar Ahmed[1] · Sudhanshu[1] · Sumit Sahil Malhotra[1] · Abdullah Saad Alsubaie[2] · Salah M. El-Bahy[3] · Ranjan Kumar Mohapatra[4] · Azaj Ansari[1]

Received: 5 August 2024 / Accepted: 20 January 2025 / Published online: 5 February 2025

Abstract

Context In the present work, DFT/TDDFT techniques is used to analyze structure, bonding, reactivity and electronic transitions of quercetin, morin, myricetin with their metal (Cu and Zn) complexes. In order to comprehend metal complexes and ligands reactivity patterns, we calculated energy gaps between frontier molecular orbitals. Global reactivity characteristics, such as ionization potential, electronegativity (χ), hardness (η), softness (S), electrophilicity index (ω) electron affinity, and chemical potential (μ), were computed based on the FMO energies. Molecular electrostatic potential (MEP) maps were used to identify nucleophilic and electrophilic sites in complexes. Within the examined complexes, TDDFT and NBO analysis shed light on bonding, electronic transitions and stabilizing interactions. Ligands morin, myricetin, and quercetin exhibited higher HOMO–LUMO gap than their corresponding metal complexes, suggesting electron transfer may be faster in the metal complexes. The metal complexes displayed more negative electrostatic potentials. The absorption spectra of the ligands ranged from 258 to 360 nm, whereas their complexes exhibited a broader range from 252 to 1035 nm. These spectra provided important insights into charge transfer and electronic transitions, enhancing our knowledge of electronic and bonding characteristics of such compounds.

Methods G16 software is used to optimize all species. B3LYP functional was employed in combination with LanL2DZ basis set for Cu and Zn, and 6-311G(d,p) basis set for other atoms (C, H and O). Natural bond orbital examination was conducted in order to investigate interactions between the filled orbitals of one unit and empty orbitals of other unit. ORCA software was utilized to compute spectral features, incorporating ZORA method to account for relativistic effects. TDDFT studies is carried out using B3LYP functional to calculate excitation energies.

Keywords Morin/myricetin/quercetin · Copper/zinc complexes · DFT/TDDFT · MEP · NBO · Bonding · Electronic transitions

Introduction

Flavonoids are natural polyphenols and are present in plant tissues namely stems, leaves, roots, seeds and fruits [1]. It is found that the primary mechanism by which flavonoids function as antioxidants is by the chelation of metal ions [2]. Because of free radicals produce metal ions through chelation, their ability to chelate metal-ions make them effective antioxidants against oxidative stress [3–5]. The metal ions facilitate the metabolic reactions that produce free radicals [6]. Because of the presence of carbonyl and hydroxyl groups, they bind with metal ions readily to form complexes [7]. The formation of chelates stops the production of free radicals mediated by metals. The flavonoids and their metal complexes' ability to scavenge free radicals

✉ Azaj Ansari
ajaz.alam2@gmail.com

1 Department of Chemistry, Central University of Haryana, Mahendergarh 123031, India

2 Department of Physics, College of Khurma University College, Taif University, 21944 Taif, Saudi Arabia

3 Department of Chemistry, Turabah University College, Taif University, P.O. Box 11099, 21944 Taif, Saudi Arabia

4 Department of Chemistry, Government College of Engineering, Keonjhar, Odisha 758002, India

and oxidants makes them suitable candidates for shielding biological systems from harm caused by radicals [8]. As a result, they have anti-inflammatory, anti-mutagenic, antioxidant, and anti-diabetic properties [9].

Among various flavonoids, morin, myricetin and quercetin are very common and shows various properties by forming metal complexes. Several fruits and herbs contain morin [10] which is extracted from different plants [11]. As seen in Fig. 1, it consists of two aromatic rings connected by an oxygen containing heterocycle. Due to its strong antioxidant and metal ion-chelating properties which come from its abundance in the human diet, it has a variety of biological and biochemical benefits, such as anti-inflammatory, anti-tumour, and cardioprotective properties [12]. The numerous results indicate that morin is a bioactive substance with a variety of biological and pharmacological characteristics and low cytotoxicity. Myricetin also falls under the group of flavonols and is mostly found in tea, fruits and vegetables [13]. This polyhydroxy flavonol molecule dissolves readily in methanol, ethanol, acetonitrile, and other polar solvents. Myricetin's properties drew particular attention because they included anti-aging, anticancer, antiplatelet aggregation, antihypertensive, immunomodulatory, anti-inflammatory, antiallergic, and analgesic properties, as well as protective effects against a variety of disorders [14].

Similar to the morin and myricetin, quercetin is also one of the most abundant flavonoids which is present in vegetables and fruits [15]. Its chemical structure consists of five ionizable hydroxyl groups and two aromatic rings connected by a g-pyrone ring. Quercetin is a powerful electron and hydrogen donor due to its many conjugated electron rich aromatic rings and ionizable hydroxyl groups. It is a popular flavonoid with marked anticancer and antioxidant activities [16]. Because of the presence of phenolic OH groups, these flavonoids structures demonstrate an amazing capacity to react with transition metal ions to generate stable metal chelates [17, 18]. It has recently been confirmed that quercetin can form stable complexes with iron, copper, zinc, ruthenium, calcium, magnesium, and aluminum [19, 20]. More antioxidant and anticancer properties were demonstrated by the majority of quercetin-based metal complexes than by quercetin alone.

Owing to their unique molecular structures, flavonoids can readily bind metal ions to form metal- complexes. Numerous investigations have demonstrated that flavonoids primarily act as antioxidants by chelating metal ions [21]. It was found that complexes of epicatechin, rutin, dihydroquercetin, with iron, copper and zinc have been discovered to be more efficient radical scavengers than free flavonoids [22]. A deeper comprehension of the intricate anti-oxidant capabilities of flavonoids is made possible by comprehending the mechanisms underlying their chelation by metal ions. Extensive experiments were conducted to comprehend the important interactions between flavonoids and metal ions, chelation sites, complex structure's reliance on metal/ligand ratio, ability of flavonoids to bind with metal ions, etc. Long-term studies on metal–flavonoid complex compounds have examined their composition. Structural characteristics, which also contribute to their pharmacological effects, various complexes that form between a specific metal and a specific flavonoid will display biological capabilities. Determining the structure of the metal-flavonoid complexes would therefore be an essential step in the production of pharmaceutical drugs. Prior to committing significant resources to extensive experiments, DFT predictions can help to identify the best stable metal flavonoid combination in a dry laboratory. The increasing interest in this type of research motivated us to investigate structure and bonding characteristics of Cu–Zn complexes of quercetin, myricetin, and morin. Motivated by such type of studies, here we have presented a thorough DFT analysis of these compounds for the first time. Thus, the goal of the current work is to anticipate metal-flavonoid structures and bonding using DFT simulations. Our goal in this work is to investigate the coordination chemistry of the ligand's quercetin, myricetin, and morin along with their metal ions, as well as their coordination modes, structural and bonding characteristics of resultant complexes and their patterns of reactivity. By conducting a thorough analysis of the coordination chemistry of the quercetin, myricetin, and morin complexes, this study intends to advance our knowledge of metal–ligand interactions and opens door for developing the novel complexes with specific functions and properties.

In this paper, we have attempted to address some important elements of the species described above: (i) electronic structures of morin, myricetin and quercetin along with their metal complexes; Cu-morin (complex 1), Zn-morin (complex 2), Cu-myricetin (complex 3), Zn-myricetin (complex 4), Cu-quercetin (complex 5) and Zn-quercetin (complex 6);

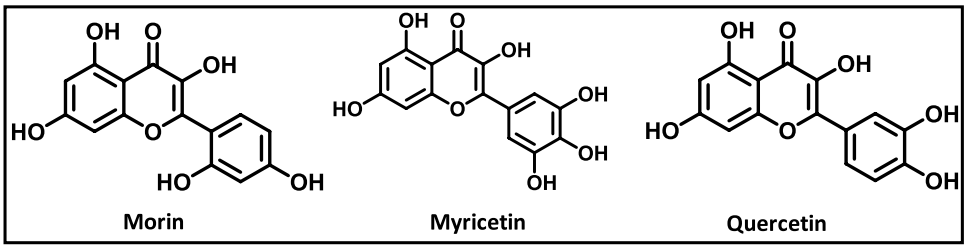

Fig. 1 Schematic representation of morin, myricetin and quercetin

(ii) Mapping of molecular electrostatic potential in order to study the charge density distribution in all molecule; (iii) Donor–acceptor interaction is studied by the analysis of natural bond order; (iv) charge transfer transitions (v) comparative analysis of all ligands and complexes.

Computational methods

Gaussian16 is utilized for optimizing all morin, myricetin and quercetin and their metal complexe [23]. In order to accurately predict the energetics and structures of complexes, we utilized unrestricted B3LYP with dispersion (D2) [24] a widely recognized DFT functional for such study [25–27]. For basis sets, we used LanL2DZ [28–30] for Cu/Zn, and 6-311G(d,p) [31] for C, H, and O atoms. These basis sets, 6-311G(d,p) and LanL2DZ, are broadly recognized for their balance between accuracy and computational efficiency in similar systems [32–36]. Geometry optimization was performed using the B3LYP functional, and frequency calculations confirmed the minima on the potential energy surface (PES) with no imaginary frequencies detected in the optimized geometries. Initial geometry modeling of the molecules was done using GaussView6.1 software [37]. GaussSum software was utilized to determine the density of states (DOS) [38]. To account for solvent effects, polarized continuum model (C-PCM) [39, 40] was employed with ethanol as the solvent, utilizing the larger basis set TZVP [41, 42]. Natural bond orbital (NBO) analysis [43, 44] was conducted to investigate interactions between filled orbitals of donor unit and empty orbitals of acceptor unit. An isosurface value of 0.03 was used for all density plots. ORCA software (version 4.0) was employed to compute spectral characteristics, incorporating zeroth order regular approximation method [45]. TDDFT calculations, using the B3LYP functional, were performed to determine excitation energies, and MO (molecular orbital) composition was examined using QMForge software [46].

Results and discussion

In our study, DFT and TDDFT calculations is conducted in order to investigate several aspects related to ligands and their complexes. Specifically, we explored structural features, bonding characteristics, charge transfer properties, distributions of molecular charge, spin density plots, natural bonding orbital analysis, density of states, and energy levels of frontier molecular orbitals. The ligands under investigation are morin, myricetin, and quercetin, along with their metal (Cu and Zn) complexes 1–6. The calculated results could contribute to establishing an insightful picture of these complexes that can be used to observe electrical and biological characteristics.

Electronic structures of ligands and metal complexes

The structures of morin, myricetin and quercetin possesses multiple hydroxyl groups, carbonyl groups and a conjugated system. The electron-donating ability of the hydroxyl groups and the conjugated system plays a key role in the biological activity of these ligands [47–49]. The ligands i.e., morin, myricetin and quercetin was optimized, and optimized structures are shown in Fig. S1 of ESI. From the Fig. S1, it is shown that computed bond lengths of C1-C2, C3-O1, C4-O2, C5-O3, C6-O4, C7-O5 and C8-O6 of morin are 1.462, 1.389, 1.390, 1.381, 1.266, 1.378, and 1.386 Å, respectively. Bond lengths of C1-C2, C3-O1, C4-O2, C5-O3, C6-O4, C7-O5 C8-O6 and C8-O7 of myricetin are 1.468, 1.391, 1.247, 1.387, 1.386, 1.400, 1.390 and 1.383 Å, respectively. Similarly, the important bond parameters of C1-C2, C3-O1, C4-O2, C5-O3, C6-O4, C7-O5 and C8-O6 of quercetin are 1.459, 1.380, 1.266, 1.377, 1.385, 1.388 and 1.400 Å, respectively. Comparative study among these ligands shows that the bond length of C1-C2 is the longest in myricetin while the lowest in quercetin.

The study of the electronic structures of metal complexes of these ligands is crucial for understanding their chemical behavior and biological activity. These ligands can form complexes with metal ions such as copper and zinc, which may alter their electronic properties and enhance their therapeutic potential [17–22, 50]. Thes ligands forms complexes with Cu^{2+} and Zn^{2+} typically involving the chelation of the copper and zinc ion by the hydroxyl and carbonyl groups present in the ligand's structure. We have optimized all the six complexes (1–6) in + 2 oxidation state of metal and the optimized geometries of all the species with significant bond parameters is shown in the Fig. 2.

The calculated bond length of Cu-O1, Cu-O2, Cu-O3, Cu-O4 of complex 1 (Cu-morin) are 1.982Å, 1.941 Å, 1.941 Å and 1.981 Å, respectively. These computed values exhibit a satisfactory level concordance with the available x-ray data 1.991 Å and 2.054 Å for M–O bonds of similar architecture [51]. Computed bond angles of O1-Cu-O2 and O3-Cu-O4 have the same value of 176.3° which suggest that the complex 1 exhibit the square planar geometry. Moreover, we have computed the spin density value of complex 1 ($\rho = 0.613$) which suggest the presence of the unpaired electron character at the copper centre (see Figs. 2a, 3a and Table S1 of ESI).

Similarly, computed bond lengths of Zn-O1, Zn-O2, Zn-O3, Zn-O4, Zn-O5 and Zn-O6 of complex 2 are 2.129, 2.119, 2.119, 2.129, 2.191 and 2.191 Å, respectively, (see Fig. 2b). From these computed bond lengths, it is concluded that the bond lengths of morin such as C3-O1 and C4-O2 get reduced on complexation with copper and zinc metals. Computed bond angles of O1-Zn-O3, O2-Zn-O4 and O5-Zn-O6

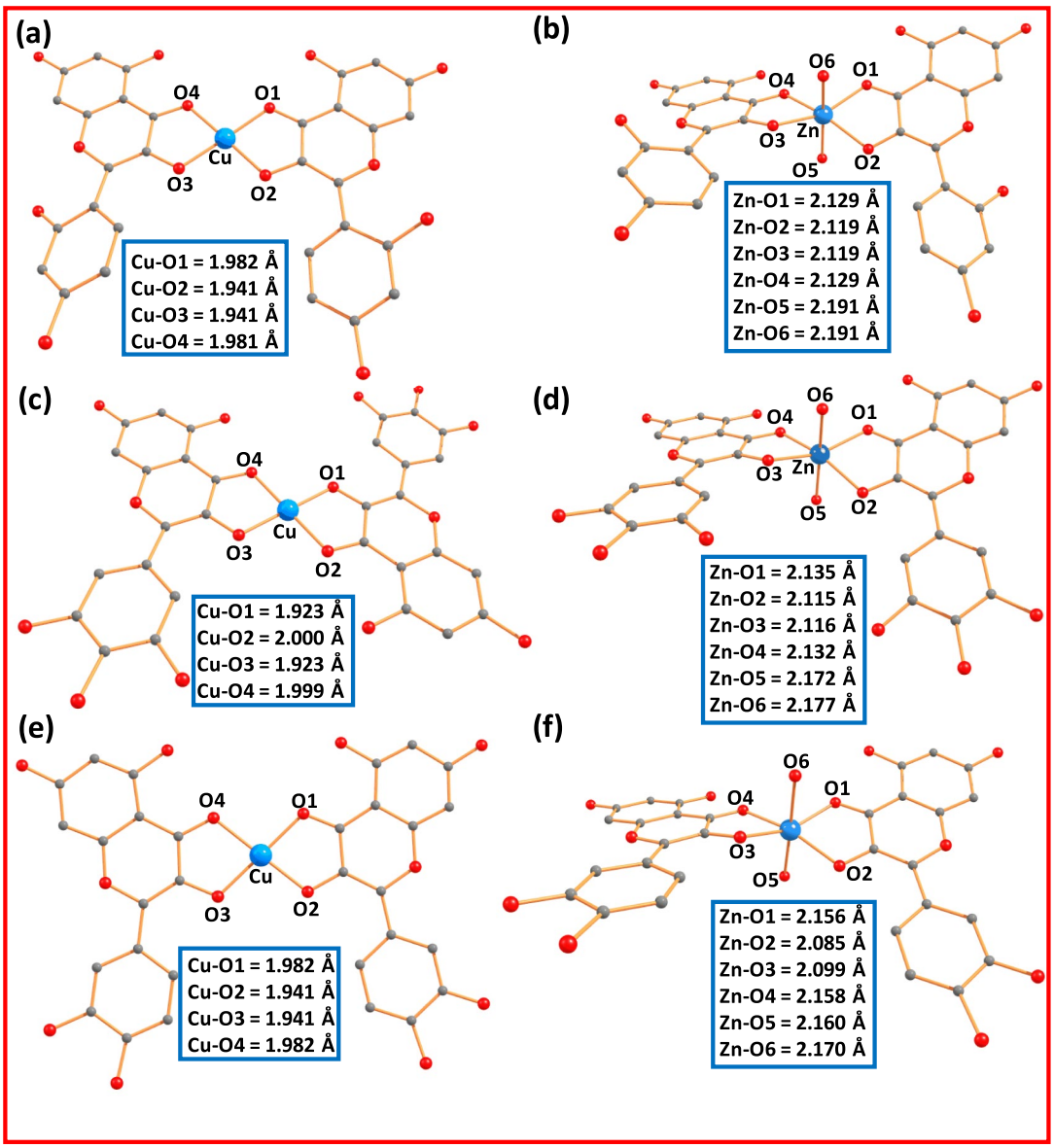

Fig. 2 Optimized structures with bond parameters of **a** Complex 1, **b** Complex 2, **c** Complex 3, **d** Complex 4, **e** Complex 5 and **f** Complex 6

are 156.4°, 156.4° and 164.2° which suggest the distorted octahedral geometry of complex 2 with presence of water molecules at the axial position. (See Table S1 in ESI).

In the similar way, we have optimized complexes 3–6 and the optimized structures are depicted in the Fig. 2c-f. Computed structural parameters of complexes show that complex 3 and 5 exhibit square planar geometry while complexes 4 and 6 as distorted octahedral. Computed spin density value of complex 3 and 5 ($\rho = 0.621$ and $\rho = 0.615$) also confirms presence of unpaired electron at copper centres (see Fig. 3b and c).

The optimized structures are shown in Fig. 2e and f. It is also observed that the bond length of C3-O1 in myricetin is decreased after complexation with metals while the bond length of C4-O2 get increased after forming the complex. Bond angles of O1-Cu-O3 and O2-Cu-O4 of complex 5 are found to be same value of 179.6° while the computed bond angles of O1-Zn-O3, O2-Zn-O4 and O5-Zn-O6 of complex 6 are 158.4°, 157.8° and 178.4°, respectively, which depicts the square planer and distorted octahedral geometry of complex 5 and 6, respectively, (see Table S1 of ESI). The unpaired electron character also indicated by spin density value ($\rho = 0.615$) at copper centre of complex 5 (see Fig. 3c). The computed bond length shows that bond length of Cu–O is shorter than corresponding Zn–O (see table S1 of ESI).

Further, analysis of frontier molecular orbital is carried out for investigating the electronic properties, charge transfer, stability, reactivity etc. of molecules [52–55]. The study

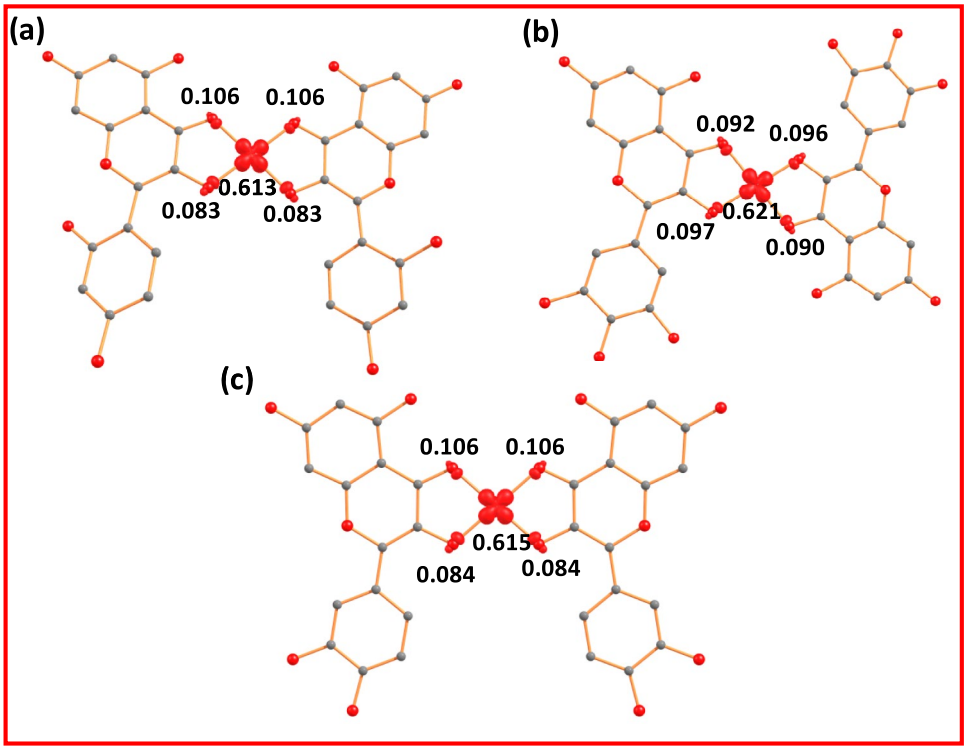

Fig. 3 Spin density plots of **a** Complex 1, **b** Complex 3 and **c** Complex 5

specifically emphasizes the importance of HOMO (highest occupied molecular orbital) and the LUMO (lowest unoccupied molecular orbital), which are important in determining chemical reactivity and molecular interactions. The energy gap between the HOMO and LUMO, known as the band gap, is a key parameter in evaluating the stability and reactivity of the molecules.

When a molecule absorbs light, electrons can jump from HOMO to LUMO which is known as electronic absorption. Electrons mostly go from the HOMO to the LUMO during electronic absorption. However, depending on the energy of the absorbed light and the particular electronic structure of the molecule, transitions between other orbitals can also happen. The energy difference between HOMO and LUMO approximates the energy required for this excitation. By comparing these gaps across different molecules, one can gain insight into their relative excitation energies and light absorption properties.

In this study, comparison of HOMO–LUMO gap for ligands morin, myricetin, and quercetin, as well as their six metal complexes is conducted. The calculated energy gaps for morin, myricetin, and quercetin are 3.96 eV, 4.15 eV, and 3.73 eV, respectively. Additionally, the computed HOMO–LUMO gaps for complexes 1 to 6 are 3.07 eV, 3.27 eV, 2.92 eV, 3.10 eV, 3.00 eV, and 3.16 eV, respectively. (see Figs. 4, 5 and 6).

The coloured lobes represent isodensity changes during the transition from HOMO to LUMO. During the transition, these lobes show how the electron density distribution changes between the two orbitals. Notable electron density at the hydroxyl and carbonyl groups in the highest occupied molecular orbitals of the ligands (see Figs. 4a, 5a, and 6a) suggests that these atoms can coordinate with metal ions to form their complexes [56]. Computed plot reveals that energy gaps of complexes are lower in comparison with ligands, indicating easier electron transfer in the metal complexes compared to the ligands. The computed energy gap of ligands and metal complexes shows that a smaller energy gap is observed in metal complexes compared to their ligands, indicates that less energy is required for electron transfer in metal complexes. This reduced energy demand allows electrons in metal complexes to be more easily excited and transferred. Among the complexes 1–6, complex 2 shows the highest gap while complex 3 has the lowest. This suggests that complex 3 may exhibit higher reactivity than the other metal complexes. Among all ligands, myricetin have the highest energy gap while quercetin have the lowest energy gap which suggest high reactivity of quercetin and high stability of myricetin.

The DFT approach provides essential insights into the stability and reactivity of molecular structures [57]. Key terms such as electron affinity (EA), ionization potential (IP), electrophilicity index (ω), electronegativity (χ), hardness (η), softness (s), and chemical potential (μ) are derived from the energies of frontier molecular orbitals, HOMO and LUMO.

These parameters help to provide crucial insights into a complex's energy, structural features, and chemical behavior,

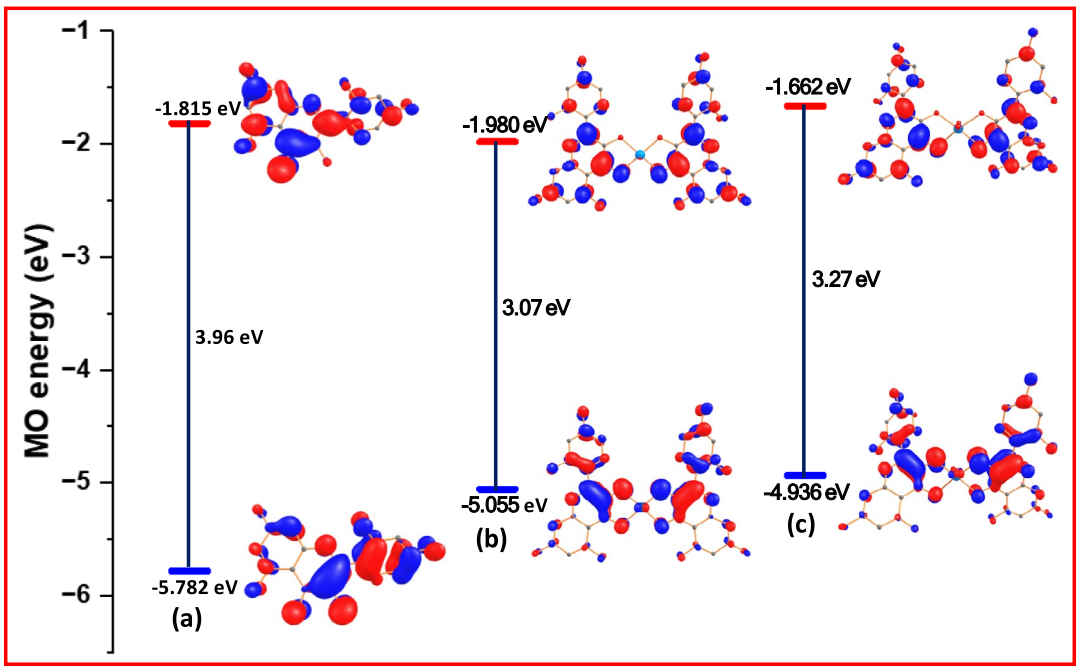

Fig. 4 Energy gap of **a** Morin **b** Complex 1 and **c** Complex 3

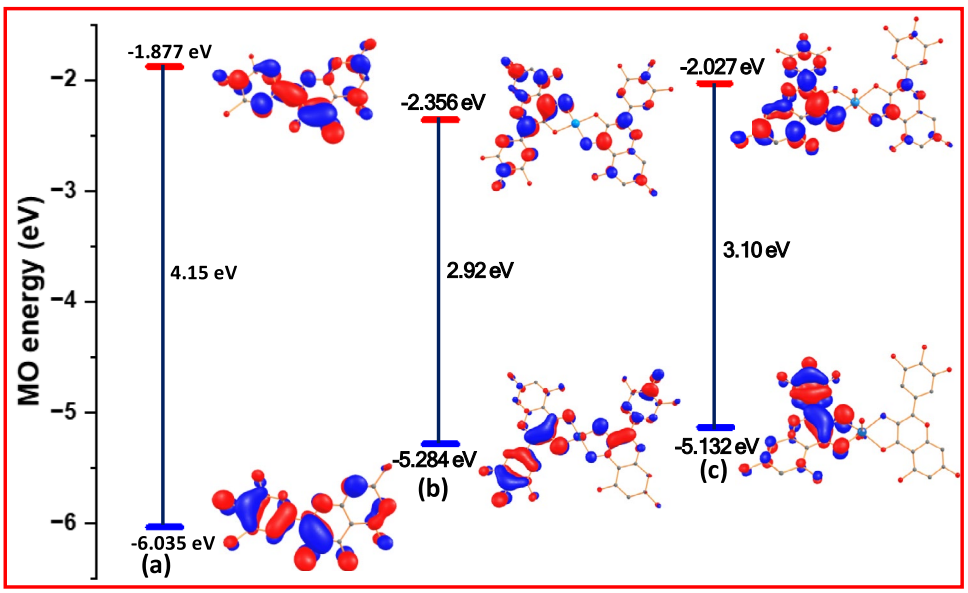

Fig. 5 Energy gap of **a** Myricetin, **b** Complex 2 and **c** Complex 4

making them valuable in quantum chemical calculations [58–63]. Koopman's theorem [58] is used for calculating the reactivity descriptors by using equations which are given in the Table S2 of ESI.

Computed reactivity parameters of ligands and complexes are presented in Table 1. The negative values of "μ" suggest that compound is thermodynamically stable and resistant to decomposition into its elemental forms, which is a key consideration in understanding its reactivity and potential applications. Their significant chemical hardness implies lower polarizability and resistance for the deformation from small perturbations. The low values of global softness rule out possibility of their being soft.

The electrophilicity index serves as a structural indicator for analyzing the chemical reactivity of molecules, reflecting their ability to accept electrons. A highly reactive nucleophile has a lower electrophilicity index (ω), while a strong electrophile is characterized by a higher value of (ω). The

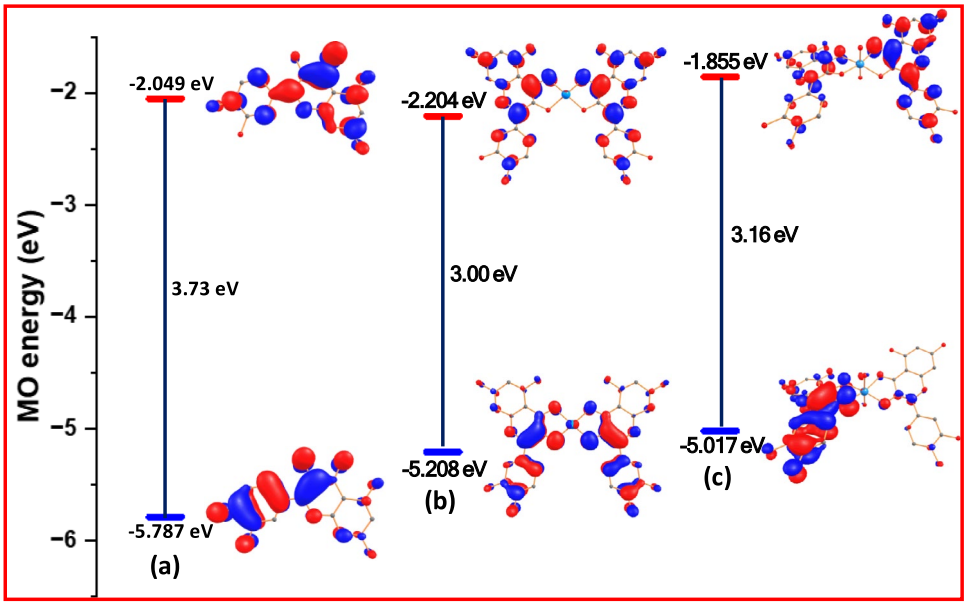

Fig. 6 Energy gap of **a** Quercetin, **b** Complex 5 and **c** Complex 6

Table 1 Computed reactivity descriptors for ligands and complexes (1–6) (values are in eV)

Ligands/Complexes	Ionization potential	Electron affinity	Chemical hardness	Chemical softness	Chemical potential	Electrophilicity index
Morin	5.782	1.814	1.984	0.252	−1.984	0.9920
Myricetin	6.035	1.877	2.079	0.240	−2.079	1.0395
Quercetin	5.782	2.040	1.870	0.267	−1.870	0.9226
Complex 1	5.055	1.980	1.537	0.325	−1.537	0.7685
Complex 2	4.936	1.66	1.635	0.305	−1.635	0.8175
Complex 3	5.28	2.35	1.463	0.341	−1.463	0.7315
Complex 4	5.13	1.97	1.578	0.316	−1.578	0.7890
Complex 5	5.20	2.20	1.502	0.332	−1.502	0.7510
Complex 6	5.01	1.85	1.577	0.316	−1.577	0.7885

results indicate that complex 3 has a less negative chemical potential (μ) compared to the other complexes, making it less reactive, whereas complex 2 has a more negative chemical potential (μ), indicating higher reactivity. Among all the ligands and the metal complexes, myricetin shows the highest negative value of chemical potential which may show higher reactivity.

The complexes being studied possess moderate values of certain parameters, likely related to their electrophilicity, nucleophilicity, chemical potential or hardness. This suggests that the complexes are neither highly electrophilic nor purely nucleophilic, indicating a balanced reactivity. Moderate values imply that the complexes can effectively participate in charge transfer without being overly reactive or inert. Consequently, "η" value of complexes is less than their individual ligands. On the other hand, the complexes' chemical softness (s) exhibits greater values, as detailed in Table 1. In practical terms, higher values correspond to increased molecular difficulty, and lower values indicate the opposite. Therefore, charge transfer processes are more readily achievable within these complexes.

To support the FMOs, we have conducted density of states (DOS) analysis [64–67], as shown in Fig. 6 and Fig. S2 of ESI. This examination provides important information on the density of states within a specific energy range. By studying frontier molecular orbitals and exploring their composition in percentages and density of states near HOMOs and LUMOs, it becomes clear that acceptor components of differing electron-withdrawing strengths can impact how electron density is spread across molecular orbitals. In the DOS illustration, the red shades represent the overall density of states, whereas the green and black shades delineate bonding and antibonding orbitals with negative energy levels, respectively.

A zero value signifies no interaction between bonding orbitals. The DOS calculations corroborate the findings concerning FMOs. Variances in acceptor groups result in distinct distribution patterns of HOMOs and LUMOs,

consequently leading to differing energy gaps between these orbitals across various molecules. The energy gaps (Eg) of morin, myricetin and quercetin are 3.96, 4.15 and 3.73 eV, respectively (see Fig. 7) Similarly, the energy gap values of metal complexes are 3.07, 3.27, 2.92, 3.10, 3.00 and 3.16 eV, respectively, (see Fig. S2. of ESI).

MEPs (Molecular electrostatic potential maps)

Molecular surface is visually represented through a molecular electrostatic potential map displaying negative and positive charge distributions. The different regions of molecules are color-coded based on their electrostatic potential: areas with the highest negative potential are marked in red, those with the highest positive potential are in blue, while regions falling between these two extremes are depicted in green and yellow hues [68–70]. Based on these MEPs, it is inferred that reddish zones signify negative potential and are likely to attack electrophilic centers, whereas blue areas are conducive to nucleophilic attacks. The yellow and green regions serve as transitional zones between the contrasting potentials. MEPs of the ligands and their six metal (Cu and Zn) complexes have been calculated here, and the results are displayed in Fig. 8. Morin, myricetin, and quercetin ligands have estimated potential values of -8.537×10^{-2}, -9.025×10^{-2}, and -8.151×10^{-2} a.u., respectively. On the other hand, the computed values of potential for the complexes 1–6 are -9.708×10^{-2}, -9.183×10^{-2}, -8.384×10^{-2}, -8.293×10^{-2}, -9.217×10^{-2} and -8.383×10^{-2} a.u., respectively (see Fig. 8). Among the ligands, morin has the most negative value of potential while quercetin has the least value. Complex 1 has the highest negative potential of all complexes, whereas complex 4 has the lowest. From the MEP analysis, it is found that the dominant color is yellowish in case of ligands, favoring the nucleophilic attack, whereas in

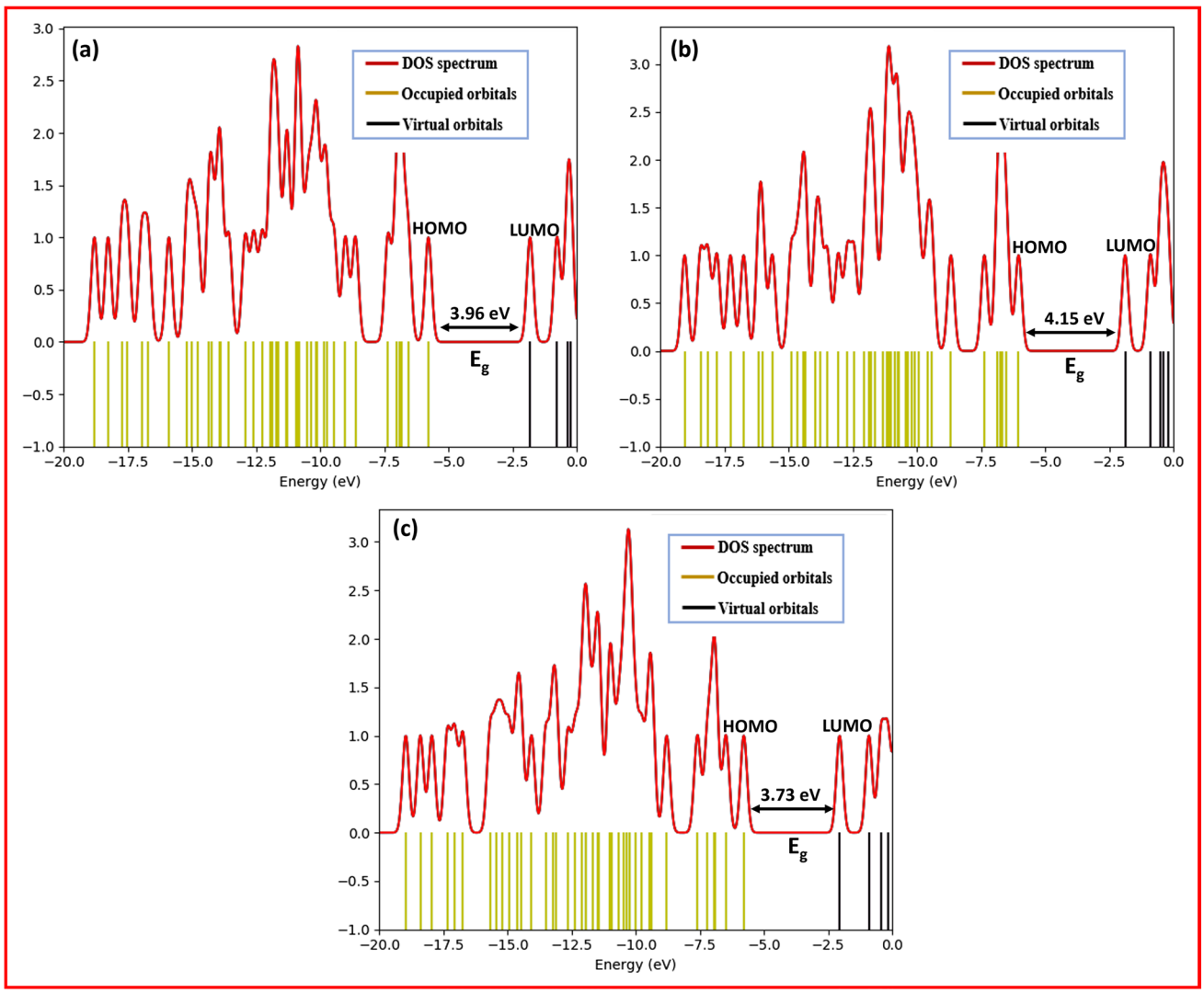

Fig. 7 Computed DOS graphs for (**a**) Morin (**b**) Myricetin and (**c**) Quercetin

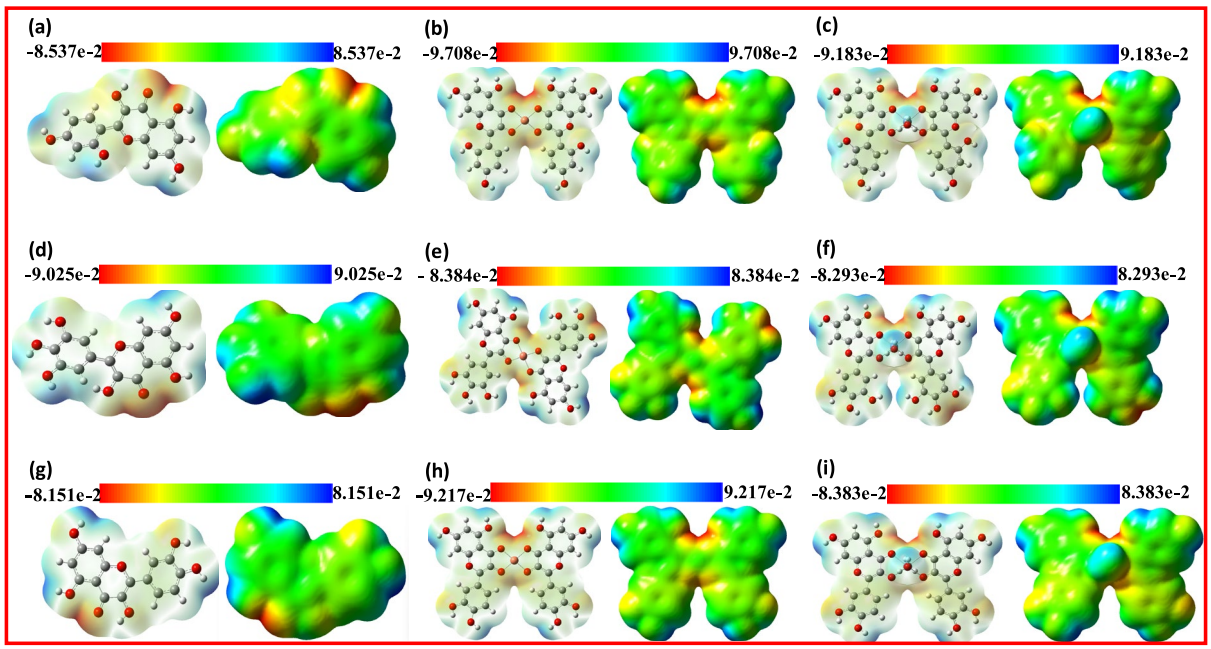

Fig. 8 Computed MEPs of **a** Morin, **b** Complex 1, **c** Complex 2, **d** Quercetin, **e** Complex 3, **f** Complex 4, **g** Quercetin, **h** Complex 5 and **i** Complex 6

case of metal complexes reddish color is dominant around the metal centres, favoring the electrophilic attack.

NBO (natural bond order) analysis

Additionally, we have performed an extensive natural bond order (NBO) [71–73] investigation of all the studied species. NBO analysis allows for the identification of localized bonds (sigma and pi) and lone pairs, which can be mapped onto the molecular structure of studied ligands. This helps to visualize the distribution of electrons in different parts of the molecule. The orbital contribution to the creation of a specific bond of the morin species is represented in Fig. 9 (position of atoms is displayed in Fig. S3(a) of ESI). For instance, in the case of morin, the percentage contribution of C1 to C2 for forming the σ-bond is depicted in Fig. 9(a), where it's evident from the data that C2 contributes more (50.18%) than C1 (49.82%). Similarly, Fig. 9(b) represents the creation of the π-bond, which arises from the overlapping of C1 (49.21%) and C2 (50.79%). The creation of the σ-bond between C3 (37.64%) and O4 (62.36%) is illustrated in Fig. 9(c). Additionally, Fig. 9(d) demonstrates the percentage contribution of O11 (66.95%) to C1 (33.05%) for forming the σ-bond, indicating that O11 contributes more than C1. Similarly, Fig. 9(e) showcases the percentage contribution of C2 (36.10%) to O21 (63.90%) for forming the σ-bond, indicating higher contribution of O21 than C2. Finally, formation of π-bond between C3 (30.31%) and O4 (69.69%), is depicted in Fig. 9(f).

In Fig. 10, the orbital contribution to the formation of specific bonds in myricetin is depicted and the figures with numbering of atoms is displayed in Fig. S3(b) of ESI. For myricetin, contribution in percentage of C1 to C2 in forming σ-bond is shown in Fig. 10(a), indicating that C1 contributes more (50.34%) than C2 (49.66%). Similarly, Fig. 10(b) illustrates the formation of the π-bond, where the overlapping of C1 (49.94%) and C2 (50.06%) occurs. Figure 10(c) showcases the formation of the σ-bond between C1 (50.09%) and C12 (49.91%). Additionally, Fig. 10(d) presents the percentage contribution of C2 to C3 for forming the σ-bond, demonstrating that C2 contributes more (52.23%) than C3 (47.77%).

Figure 11 provides insights into the orbital contributions in forming specific bonds within the quercetin species (position of atoms is displayed in Fig. S3(c) of ESI. In the case of quercetin, percentage contribution of C1 to C2 in forming the σ-bond is depicted in Fig. 11(a), revealing that C2 contributes more (50.08%) than C1 (49.92%). Similarly, Fig. 11(b) illustrates the formation of the π-bond, where the overlapping of C1 (49.22%) and C2 (50.78%) is evident. Figure 11(c) illustrates the formation of the σ-bond between C1 (32.79%) and O10 (67.21%). Additionally, Fig. 11(d) shows the percentage contribution of C1 to C15 for forming the σ-bond, indicating that C1 contributes more (50.59%) than C15 (49.41%).

Second-order perturbation analysis

The investigation of donor-receptor interactions within ligands and their metal-complexes is carried out by employing second

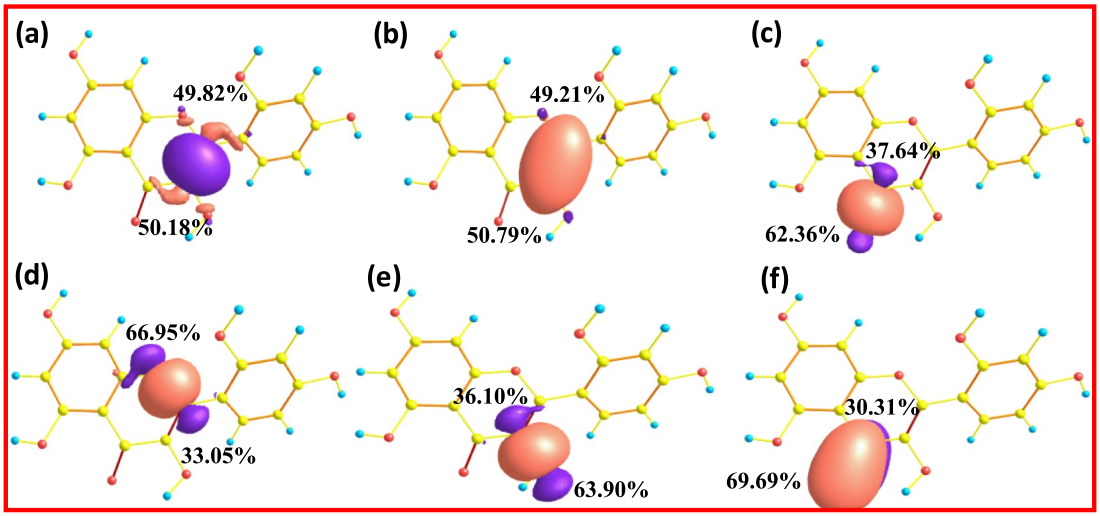

Fig. 9 NBO plots along with the orbital contributions of Morin (**a**-**f**)

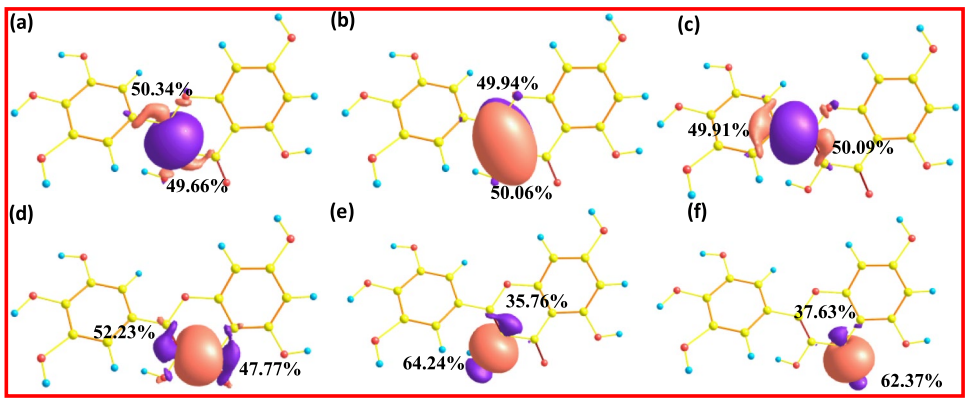

Fig. 10 NBO plots along with the orbital contributions of Myricetin (**a**-**f**)

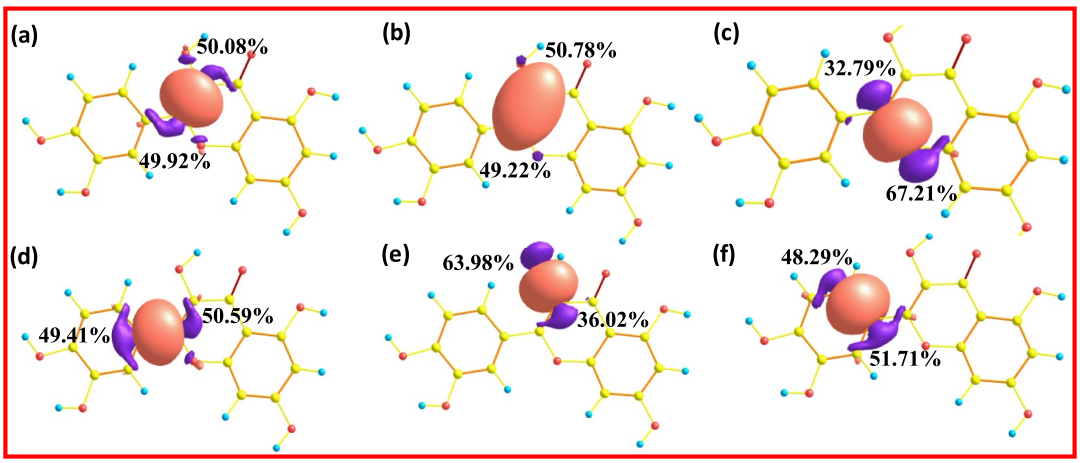

Fig. 11 NBO plots along with the orbital contributions of Quercetin (**a**-**f**)

Table 2 Computed excitation energy (cm^{-1}), oscillator strengths, electronic transitions assignment and nature of the transitions of complexes 1–6

Wavelength (λ in nm)	Excitation energy (cm^{-1})	Oscillation strength *(f)*	Transitions assignment	Nature of transition
Complex-1				
252	39590.3	0.01	H-12 (β) → L + 2 (β) (49.0%)	MLCT
275	36450.3	0.16	H (β) → L + 5(β) (15.5%)	LLCT
300	33536.0	0.47	H-12 (β) → L (β) (49.0%)	MMCT
388	25776.1	1.02	H-1(β) → L + 1 (β) (29.7%)	LLCT
444	22437.7	0.05	H (β) → L + 1 (β) (50.4%)	
Complex-2				
259	38873.8	0.39	H-1 (α) → L + 8 (α) (12.7%)	LMCT
277	35852.7	0.23	H (α) → L + 1 (α) (12.4%)	LLCT
303	33096.1	0.02	H-1 (α) → L + 2 (α) (18.5%)	
322	31053.2	0.01	H-2 (α) → L (α) (24.6%)	
387	25906.6	0.01	H (α) → L + 1 (α) (23.8%)	
Complex-3				
260	38335.6	0.03	H (β) → L + 8 (β) (25.9%)	LLCT
275	36265.2	0.07	H-9 (β) → L + 2 (β) (35.3%)	
301	33126.1	0.28	H (α) → L + 2 (α) (14.0%)	
330	30303.5	0.13	H-10 (β) → L (β) (78.0%)	MMCT
347	28652.6	0.08	H-4 (α) → L (α) (28.5%)	LLCT
401	24985.3	0.80	H-1 (β) → L + 2 (β) (26.5%)	
540	18536.3	0.08	H (β) → L + 1 (β) (39.4%)	
Complex-4				
263	38091.5	0.09	HOMO-7(β) → LUMO + 1(β) (47.4%)	LLCT
280	35808.9	0.03	H (α) → L + 4 (α) (27.8%)	
337	29,649.1	0.03	H-4 (α) → L (α) (17.5%)	
390	25,620.4	0.01	H-1 (α) → L + 1 (α) (13.0%)	
Complex-5				
428	23359.0	0.35	H (α) → L + 18 (α) (49.2%)	LLCT
478	20927.0	0.27	H-5 (α) → L + 4 (α) (17.7%)	
568	17550.0	0.03	H-20 (β) → L (β) (28.2%)	LMCT
665	15076.2	0.08	H (α) → L + 7 (α) (17.6%)	LLCT
768	13086.0	0.02	H-3 (β) → L + 2 (β) (61.2%)	
1035	9624.5	0.09	H-2 (β) → L + 3 (β) (15.5%)	
Complex-6				
258	38723.0	0.32	H-10 (α) → L + 1 (α) (8.18%)	LMCT
277	36140.7	0.28	H-7 (α) → L + 1 (α) (18.1%)	LLCT
332	30117.2	0.08	H-2 (α) → L (α) (25.4%)	
388	25788.7	1.05	H (α) → L + 1 (α) (22.4%)	

order perturbation methods utilizing NBO analysis. This analysis yields valuable insights into orbital strength and bonding and interaction within the molecules [74, 75]. Stabilization energy is calculated for both acceptor and donor natural bond orbitals [76]. The "interaction stabilization energy," E(2), resulting from electron delocalization between donor (i) and acceptor (j) pair, is calculated using the equation given below:

$$E^{(2)} = \mathbf{q}_i \frac{F^2(i,\ j)}{\varepsilon_j - \varepsilon_j}$$

In this case, donor orbital's occupancy is denoted by qi, diagonal elements are represented by Ɛi and Ɛj, and the off-diagonal NBO Fock matrix element is shown by F (i, j).

Different types of interactions are observed in these complexes which are explained here along with their stabilization energies. In Complex 1, the donor–acceptor interaction involves transitions from π(C1-C2) to n*(C3), π(C7-C8) to π*(C4-C9), π(C15-C16) to π*(C19-C20), n*(C3) to π*(C1-C2), n*(C3) to π*(C4-C9), with computed stabilization energies of 26.69, 17.81, 17.03, 20.52, and 28.35 kcal/mol, respectively (see Fig. S4 and Table S3 in ESI). Similarly,

in complex 2, interactions such as π(C1-C2) to n(C15), n(C1-C2) to π*(C3-O11), π*(C3-O11) to π*(C1-C2), and n(O10) to π*(C4-C9) are observed, with corresponding stabilization energies of 25.51, 31.75, 76.85, and 40.53 kcal/mol, respectively (see Fig. S5 and Table S4 in ESI).

In a similar manner, the complexes of myricetin with copper and zinc has their stabilization energy calculated. Table S5 and S6 of ESI lists the different transitions found in complex 3 and complex 4 along with the stabilization energy. The donor–acceptor interaction in Cu-myricetin (complex 3) is calculated between π*(C31–C36) to π*(C34–C35), π*(C4–C9) to π*(C5–C6), π*(C15–C16) to n*(C17), n(O38) to n*Cu and n(O41) to n*Cu. The computed stabilization energies are 196.47, 108.84, 36.81, 19.43, and 24.71 kcal/mol, respectively (see Fig. S6 and Table S5 of ESI).

Zn-myricetin (complex 4) contains a number of intense interactions including π*(C31-C36) to π*(C30-O38), n(O14) to π*(C1-C2), n(O41) to π*(C28-C29), n(O55) to n*Zn, and n(O57) to n*Zn, with stabilization energies of 40.34, 52.89, 52.55, 54.15, and 55.10 kcal/mol, respectively (see Fig. S7 and Table S6 of ESI).

Furthermore, bonding with copper in complex-5 (Cu-quercetin) involves stabilization through various donor–acceptor interactions including n(O42) to n*(Cu), π(C1-C2) to π*(C3-O11), n(O11) to n*(Cu), and π*(C4-C9) to π*(C5-C6), with respective energy values of 17.63, 17.38, 19.98, and 125.72 kcal/mol. (refer to Fig. S8 and Table S7 of ESI). Similarly, strong donor–acceptor interactions are also shown by Zn-quercetin, which helped to stabilise the ligand and metal connections. With an energy of 311.20 kcal/mol, the highest delocalization is found from π*(C4-C9) to π*(C5-C6). Other interactions like n(O10) to π*(C1-C2), n(O11) to n*(Zn), and π(C1-C2) to π*(C3-C11) are also present with the stabilization energy values of 25.84, 26.50 and 31.26 kcal/mol, respectively. Other different donor–acceptor interactions as well as the stabilisation energies that were calculated for complex 6 are shown in Fig. S9 and Table S8 of ESI.

TDDFT study

To learn more comprehensively about active sites and electronic transitions of complexes, we have computed TDDFT of morin, myricetin, quercetin, and their metal complexes

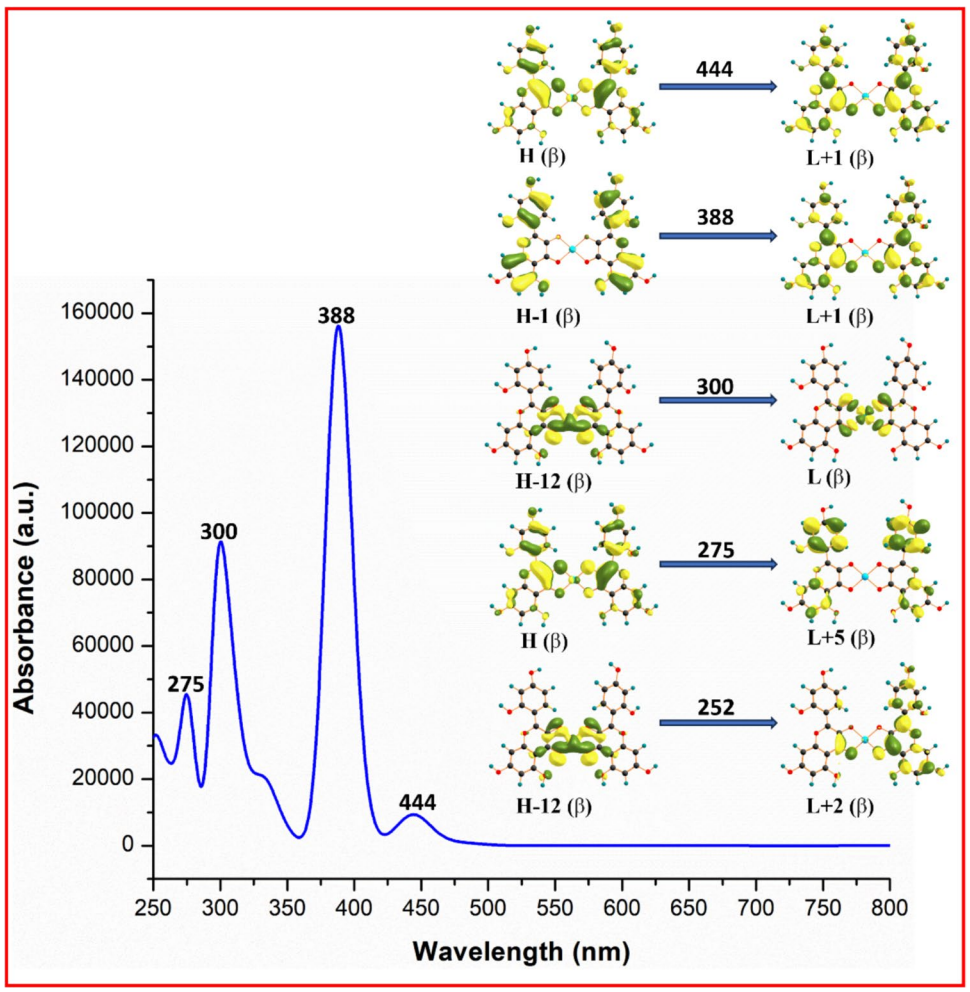

Fig. 12 Electronic absorption spectrum of Complex 1

(1–6) with the lowest 150 vertical excited states' transition energies [77–82].

Table 2 presents significant oscillator strengths, absorption peaks, and their corresponding distinctive characteristics. Three peaks can be seen in the morin absorption spectrum at 258, 306, and 351 nm (see Fig. S10 of ESI). At 258 nm, isodensity is more crowded on aromatic rings and -OH groups which correspond to transition from H(α) to L(α). Similarly, the myricetin shows four peaks at 261, 285, 324 and 345 nm (see Fig. S11 of ESI). The peak at 345 nm with highest oscillator strength correspond to the transition from H(α) to L(α) (H: HOMO and L: LUMO). In case of the quercetin, five different peaks were observed with different value of oscillator strength (see Fig. S12 of ESI). The peak at 360 nm with highest oscillation strength correspond to the transition from H(α) to L(α). The other four peaks at 260, 282, 311 and 332 nm with moderate oscillation strength (see Fig. S12 of ESI).

Figures 12, 13, 14, 15, 16 and 17 depicts the absorption peaks and associated molecular orbitals involved in electronic transitions for copper and zinc complexes (1–6). Specifically, TDDFT computed absorption spectra of complex 1 reveals five peaks at 252, 275, 300, 388, and 444 nm, corresponding to transitions from H-12 (β) to L + 2 (β), H (β) to L + 5 (β), H-12 (β) to L (β), H-1 (β) to L + 1 (β), and H (β) to L + 1 (β), respectively, (see Fig. 12 and Table 2). Notably, peak at 300 nm, with oscillator strength of 0.47, predominantly involves H-12 (β) to L (β), contributing 49.0% to this transition. The 252 nm peak signifies a metal to ligand charge transfer, while 300 nm peak indicates metal to metal charge transfer, with remaining peaks representing ligand to ligand charge transfer transitions. Similarly, absorption spectra for Zn-morin (complex 2) illustrates five peaks at 259, 277, 303,322, and 387 nm. The 259 nm peak corresponds to a ligand to metal charge transfer, with a 12.7% contribution from H-1 (α) to L + 8 (α). The subsequent peaks at 277, 303, 322, and 387 nm signify ligand to ligand charge transfer transitions, involving H (α) to L + 1 (α), H-1 (α) to L + 2 (α), H-2 (α) to L(α), and H(α) to L + 1 (α), respectively, (see Fig. 13).

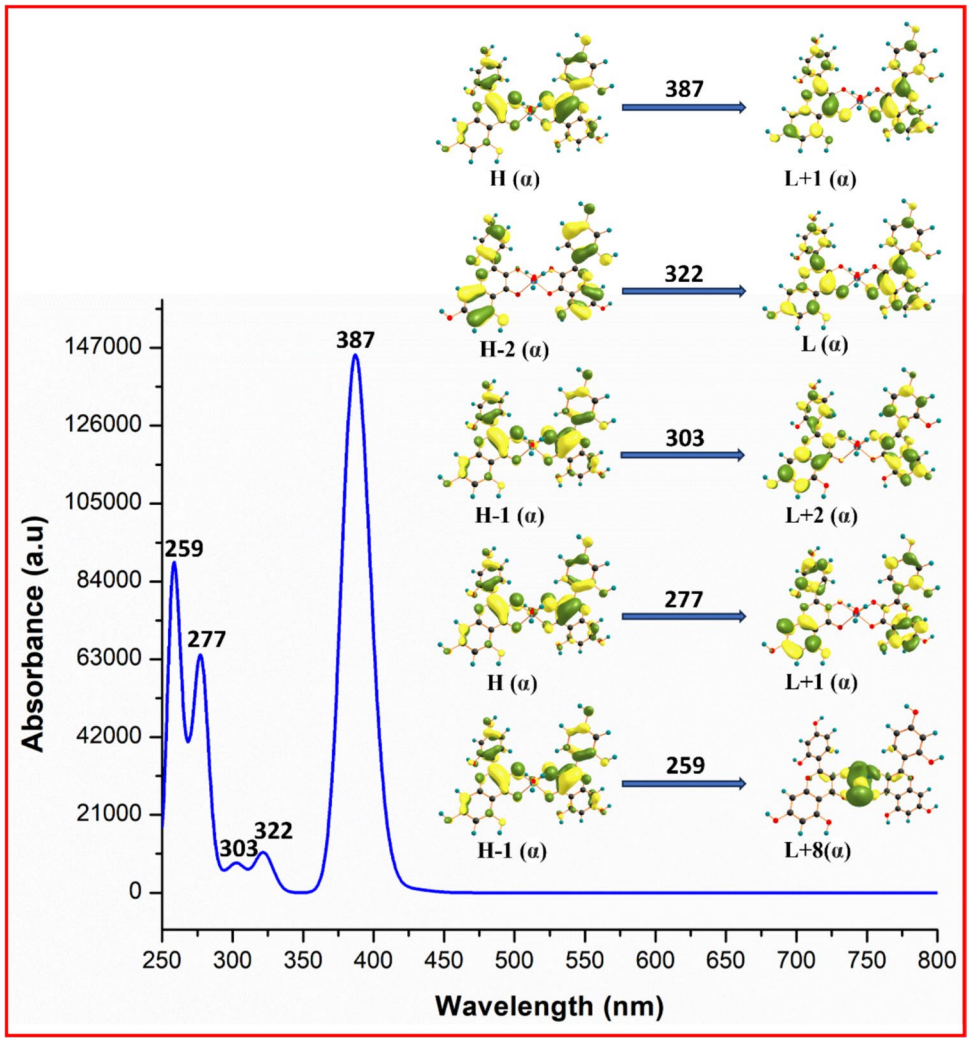

Fig. 13 Electronic absorption spectrum of Complex 2

Computed absorption spectra of complexes 3 and 4 also show peaks in the 260–540 nm region, which are often associated with charge transfer transitions from metal to ligand and ligand to ligand. Further, complex 3 exhibits seven peaks at 260, 275, 301, 330, 347, 401, and 540 nm, as shown in Fig. 14. The peaks at 260, 275, 301, 347, 401, and 540 nm correspond to H (β) to L + 8 (β) (25.9%), H-9 (β) to L + 2 (β) (35.3%), H (α) to L + 2 (α) (14.0%), H-4 (α) to L (α) (28.5%), H-1 (β) to L + 2 (β) (26.5%), and H (β) to L + 1 (β) (39.4%), respectively, indicating ligand to ligand charge transfer. Also peak at 330 nm, corresponding to H-10 (β) to L (β) (78.0%), indicates a metal-to-metal charge transfer. While complex 4 also exhibits ligand to ligand charge transfer at peaks 263, 280, 337, and 390 nm, corresponding to transitions from H-7 (β) to L + 1 (β), H (α) to L + 4 (α), H-4 (α) to L (α), and H-1 (α) to L + 1 (α), respectively (see Fig. 15).

Six distinct spectral peaks are evident for complex 5, appearing at wavelengths of 428, 478, 568, 665, 768, and 1035 nm, as depicted in Fig. 16. Notably, a prominent spectral peak at 568 nm, with oscillator strength of 0.03, is predominantly attributed to a 28.2% contribution from the H-20 (β) to L (β) transition, suggesting an anticipated ligand-to-metal charge transfer. Remaining five peaks, observed at 428, 478, 665, 768, and 1035 nm, signify ligand-to-ligand charge transfer processes, with respective contributions of 49.2%, 17.7%, 17.6%, 61.2%, and 15.5%. Specifically, these transitions involve H (α) to L + 18 (α), H-5 (α) to L + 4 (α), H (α) to L + 7 (α), H-3 (β) to L + 2 (β), and H-2 (β) to L + 3 (β). All five peaks are indicative of ligand to ligand charge transfer phenomena.

The complex 6 exhibits four peaks at 258, 277, 332, and 388 nm, as shown in Fig. 17. First peak at 258 nm, involving an 8.18% contribution from the H-10 (α) to L + 1 (α) transition, indicates ligand-to-ligand charge transfer. Subsequent peaks at 277, 332, and 388 nm correspond to transitions from H-7 (α) to L + 1 (α), H-2 (α) to L (α), and H (α) to L + 1 (α), respectively, all of which also indicate ligand-to-ligand charge transfer.

Comparative study

Using DFT and TDDFT techniques, we examined structures, bonding, and electronic transitions of zinc and copper complexes containing the ligands quercetin, myricetin, and morin. Among copper complexes, complex 1 has the highest spin density delocalization (ρ = 0.613). Across all the species, complex 3 has the lowest HOMO–LUMO gap, whereas myricetin has the highest, indicating that myricetin is more reactive than morin and quercetin. Among the complexes, complex 2 has the highest gap, while complex 3 has the lowest, suggesting that complex 3 may be more reactive. These findings are corroborated by density of state analysis. Molecular electrostatic potential (MEP) plots revealed that complex 1 exhibited the most

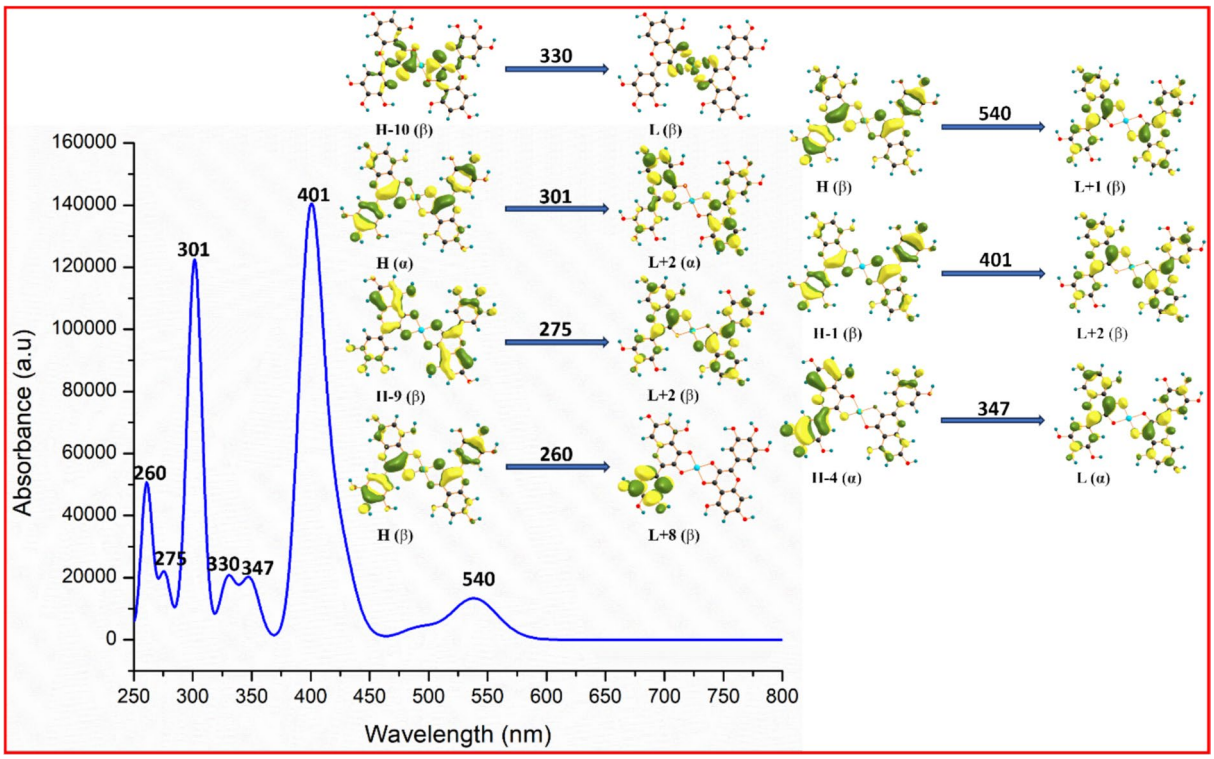

Fig. 14 Electronic absorption spectrum of Complex 3

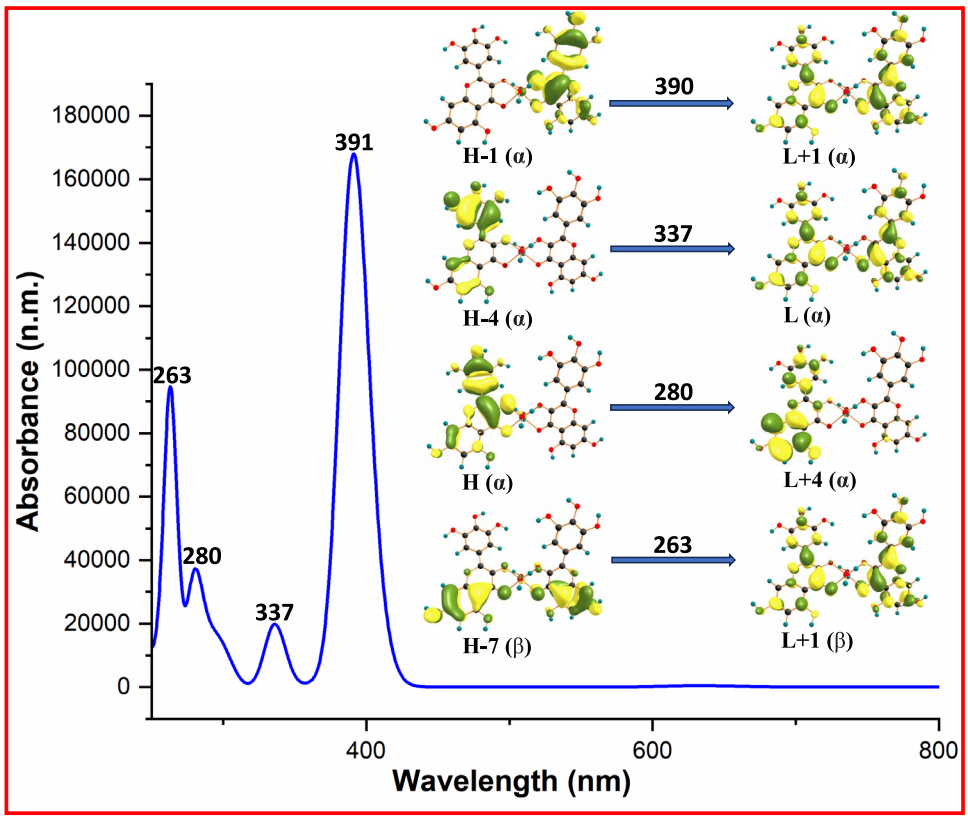

Fig. 15 Electronic absorption spectrum of Complex 4

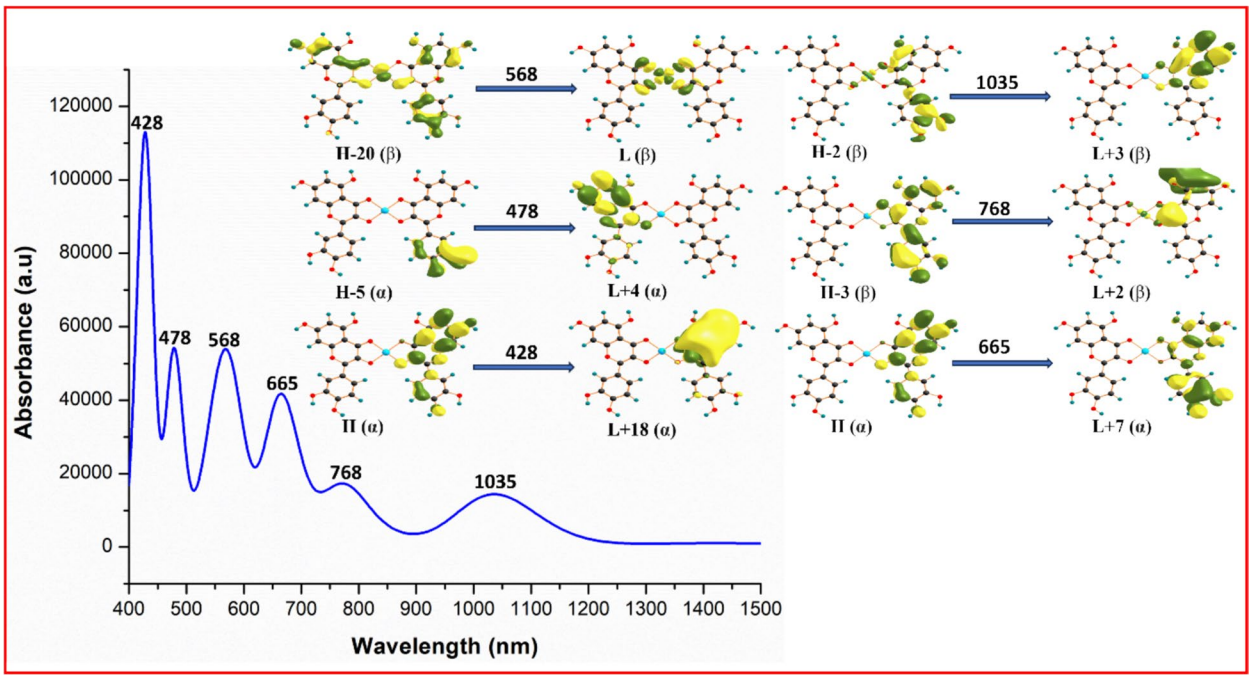

Fig.16 Electronic absorption spectrum of Complex 5

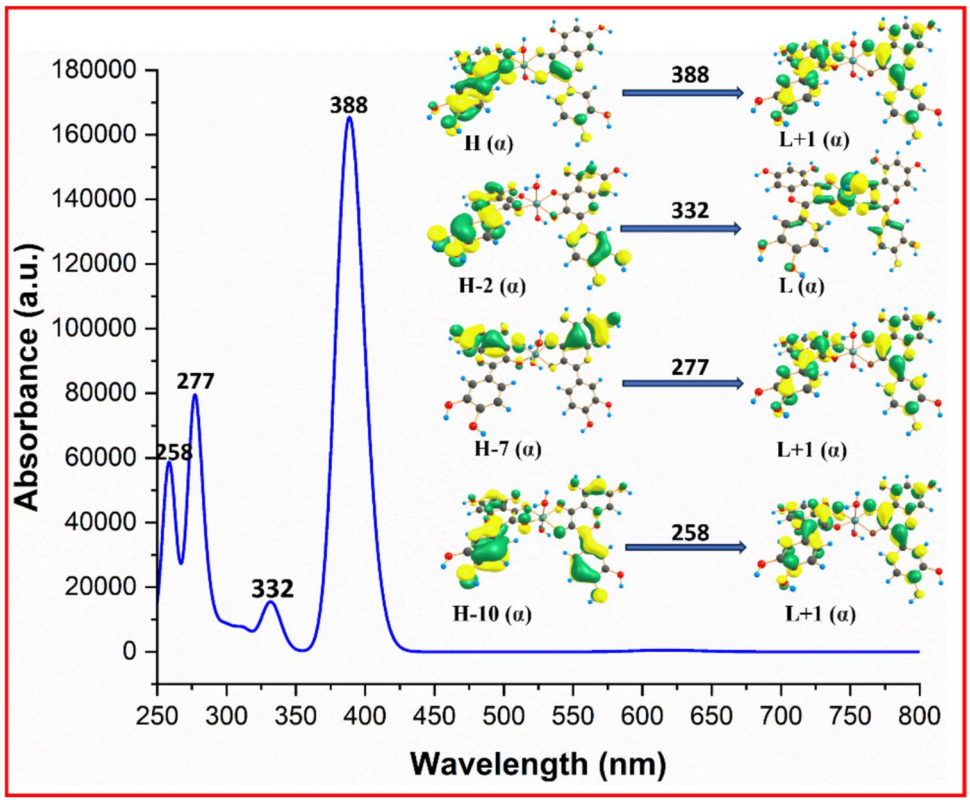

Fig.17 Electronic absorption spectrum of Complex 6

pronounced negative potential, while quercetin showed the least value of negative potential. Among metal complexes, complex 1 has the most negative potential value, and complex 4 has the least value.

In TDDFT simulations the complexes predominantly exhibit metal-to-ligand charge transfer (MLCT) and ligand-to-ligand charge transfer (LLCT) transitions. The absorption spectra of these complexes span a range of wavelengths from 252 to 1035 nm. Among the ligands, each shows a prominent peak with the highest oscillator strength compared to the other peaks. Notably, complex 5 has peaks at higher wavelengths i.e., 665 nm, 768 nm, and 1035 nm that are absent in the other complexes, which display peaks within the 250 nm to 540 nm range. Complexes 1, 2, 3, 4 and 6 exhibit peaks ranging from 252 to 401 nm, with 3 showing a peak at 540 nm. On the other hand, as we move from complex 4 to 5 peaks can be seen at longer wavelengths. Complex 6 shows peaks in the 428 nm to 1035 nm range, distinct from the other complexes. The stabilization of the complexes is proposed to result from dominant interactions between donors and acceptors. The ligands and their metal complexes are stabilized by several interactions, such as $\pi \rightarrow \pi^*$, $\sigma \rightarrow \pi^*$, $n \rightarrow \pi^*$ and $n \rightarrow n^*$. Of these, the $n \rightarrow n^*$ interaction is consistently found in all the metal complexes and is the primary interaction observed.

Conclusions

This report delves into the electronic and bonding characteristics of morin, myricetin, and quercetin, as well as their complexes with copper and zinc. Computed parameters reveal square planar and distorted octahedral geometries for copper and zinc complexes, respectively. The HOMO–LUMO gap of the ligands suggests the higher reactivity of quercetin compared to morin and myricetin, while their metal complexes exhibit reduced energy gaps, implying high reactivity. Among these complexes, complex 2 demonstrates a larger energy gap, potentially indicating lower reactivity. Reactive parameters derived from HOMO and LUMO energies unveil distinct characteristics such as hardness, softness, and chemical potential etc. Myricetin is found to be more capable of nucleophilic attack than both quercetin and morin based on MEP plots. Furthermore, in comparison to the other complexes, the complex 1 (Cu-morin) complex may be more vulnerable to nucleophilic attack as revealed by MEP maps. TDDFT simulations elucidate charge transfer transitions, providing insights into the specific molecular orbitals involved. LMCT, MLCT, and LLCT contribute to the stabilization of copper and zinc complexes with morin, myricetin, and quercetin, as revealed by TDDFT calculations. NBO analysis further delineates various interactions contributing to species stability, including $\pi \rightarrow \pi^*$, $\sigma \rightarrow \pi^*$, $n \rightarrow n^*$, and $n \rightarrow \pi^*$ interactions.

Supplementary Information The online version contains supplementary material available at https://doi.org/10.1007/s00894-025-06296-w.

Acknowledgements MA and SSM would like to thank the HSC SIT and Central University of Haryana for the financial support. AA would like to thank the Central University of Haryana for providing computing facilities. The authors extend their appreciation to Taif University, Saudi Arabia, for supporting the work through project number (TU-DSPP-2024-20).

Authors contribution DFT calculations, validation, methodology, writing-original draft preparation: Mukhtar Ahmed, TDDFT calculations, data analysis: Sudhanshu, NBO, MEP, DOS, visualisation: Sumit Sahil Malhotra, Conceptualization, funding acquisition: Abdullah Saad Alsubaie, Funding acquisition, analysis and interpretation of results: Salah M. El-Bahy, Writing—review and editing; Ranjan Kumar Mohapatra, Resources, formal analysis, editing and supervision: Azaj Ansari. All authors have critically reviewed and approved the final draft.

Funding This research was funded by Taif University, Saudi Arabia, Project No. (TU-DSPP-2024-20).

Data availability No datasets were generated or analysed during the current study.

Declarations

Ethical approval Not applicable.

Consent to participate Not applicable.

Consent for publication All authors provided consent to publish.

Competing interests The authors declare no competing interests.

References

1. Lee HJ, Kerr RA, Korshavn KJ et al (2016) Effects of hydroxyl group variations on a flavonoid backbone toward modulation of metal-free and metal-induced amyloid-β aggregation. Inorg Chem Front 3:381–392. https://doi.org/10.1039/c5qi00219b
2. Korkina LG, Afanas'ev IB (1997) Antioxidant and chelating properties of flavonoids. Adv Pharmacol (San Diego, Calif) 38:151–163. https://doi.org/10.1016/s1054-3589(08)60983-7
3. Edewor TI, Agboola PO, Amuda MO et al (2023) Total phenolic, flavonoid and mineral contents of the methanolic leaf extract of parinari curatellifolia planch ex benth. Int J Chem Res 7:13–18. https://doi.org/10.22159/ijcr.2023v7i2.218
4. Mercado-Mercado G, de la Rosa LA, Alvarez-Parrilla E (2020) Effect of pectin on the interactions among phenolic compounds determined by antioxidant capacity. J Mol Struct 1199:126967. https://doi.org/10.1016/j.molstruc.2019.126967
5. Adusei-Gyamfi J, Ouddane B, Rietveld L et al (2019) Natural organic matter-cations complexation and its impact on water treatment: A critical review. Water Res 160:130–147. https://doi.org/10.1016/j.watres.2019.05.064
6. Fenton HJH (1894) LXXIII.—Oxidation of tartaric acid in presence of iron. J Chem Soc Trans 65:899–910. https://doi.org/10.1039/ct8946500899
7. Malesev D, Kuntic V (2007) Investigation of metal-flavonoid chelates and the determination of flavonoids via metal-flavonoid complexing reactions. J Serb Chem Soc 72:921–939. https://doi.org/10.2298/jsc0710921m
8. Šimunková M, Valko M, Bučinský L, Malček M (2020) Structure functionality relationship of flavonoids (myricetin, morin, taxifolin and 3′,4′-dihydroxyflavone). A computational study via the cupric ion probe. J Mol Struct 1222:128923–128923. https://doi.org/10.1016/j.molstruc.2020.128923
9. Khairinisa MA, Latarissa IR, Athaya NS et al (2023) Potential application of marine algae and their bioactive metabolites in brain disease treatment: pharmacognosy and pharmacology insights for therapeutic advances. Brain Sci 13:1686–1686. https://doi.org/10.3390/brainsci13121686
10. Al-Numair KS (2012) Morin, a flavonoid, prevents lysosomal damage in experimental myocardial ischemic rats. J Med Plant Res 6:3445–3449. https://doi.org/10.5897/jmpr11.1760
11. Caselli A, Cirri P, Santi A, Paoli P (2016) Morin: A promising natural drug. Curr Med Chem 23:774–791. https://doi.org/10.2174/0929867323666160106150821
12. Guo Y, Peng X, Liu F et al (2024) Potential of natural products in inflammation: biological activities, structure–activity relationships, and mechanistic targets. Arch Pharmacal Res. https://doi.org/10.1007/s12272-024-01496-z
13. Semwal D, Semwal R, Combrinck S, Viljoen A (2016) Myricetin: A dietary molecule with diverse biological activities. Nutrients 8:90. https://doi.org/10.3390/nu8020090
14. Tsao R (2010) Chemistry and biochemistry of dietary polyphenols. Nutrients 2:1231–1246. https://doi.org/10.3390/nu2121231
15. Apak R, Güçlü K, Demirata B et al (2007) Comparative evaluation of various total antioxidant capacity assays applied to phenolic compounds with the CUPRAC assay. Molecules 12:1496–1547. https://doi.org/10.3390/12071496
16. Kumar S, Pandey AK (2013) Chemistry and biological activities of flavonoids: An overview. Sci World J 2013:1–16. https://doi.org/10.1155/2013/162750
17. Ravichandran R, Rajendran M, Devapiriam D (2014) Antioxidant study of quercetin and their metal complex and determination of stability constant by spectrophotometry method. Food Chem 146:472–478. https://doi.org/10.1016/j.foodchem.2013.09.080
18. Lakshmi BA, Bae J-Y, An JH, Kim S (2019) Facile design and spectroscopic characterization of novel bio-inspired Quercetin-conjugated tetrakis (dimethylsulfoxide)dichlororuthenium(II) complex for enhanced anticancer properties. Inorganica Chim Acta 495:118989. https://doi.org/10.1016/j.ica.2019.118989
19. Corrente GA, Malacaria L, Beneduci A et al (2021) Experimental and theoretical study on the coordination properties of quercetin towards aluminum(III), iron(III) and copper(II) in aqueous solution. J Mol Liq 325:115171–115171. https://doi.org/10.1016/j.molliq.2020.115171
20. Halevas E, Mavroidi B, Pelecanou M, Hatzidimitriou AG (2021) Structurally characterized zinc complexes of flavonoids chrysin and quercetin with antioxidant potential. Inorganica Chim Acta 523:120407–120407. https://doi.org/10.1016/j.ica.2021.120407
21. Kasprzak MM, Erxleben A, Ochocki J (2015) Properties and applications of flavonoid metal complexes. RSC Adv 5:45853–45877. https://doi.org/10.1039/C5RA05069C
22. Kostyuk VA, Potapovich AI, Vladykovskaya EN et al (2001) Influence of metal ions on flavonoid protection against asbestos-induced cell injury. Arch Biochem Biophys 385:129–137. https://doi.org/10.1006/abbi.2000.2118
23. Frisch MJ, Trucks GW, Schlegel HB, Scuseria GE, Robb MA, Cheeseman JR, Montgomery Jr JA, Vreven T, Kudin KN, Burant JC, Millam JM, Iyengar SS, Tomasi J, Barone V, Mennucci B, Cossi M, Scalmani G, Rega N, Petersson GA, Nakatsuji H, Hada M, Ehara M, Toyota K, Fukuda R, Hasegawa J, Ishida M, Nakajima T, Honda Y, Kitao O, Nakai H , Klene M, Li X, Knox JE, Hratchian HP, Cross JB, Bakken V, Adamo C,

Jaramillo J, Gomperts R, Stratmann RE, Yazyev O, Austin AJ, Cammi R, Pomelli C, Ochterski JW, Ayala PY, Morokuma K, Voth GA, Salvador P, Dannenberg JJ, Zakrzewski VG, Dapprich S, Daniels AD, Strain MC, Farkas O, Malick DK, Rabuck AD, Raghavachari K, Foresman JB, Ortiz JV, Cui Q, Baboul AG, Clifford S, Cioslowski J, Stefanov BB, Liu G, Liashenko A, Piskorz P, Komaromi I, Martin RL, Fox DJ, Keith T, Al-Laham MA, Peng CY, Nanayakkara A, Challacombe M, Gill PMW, Johnson B, Chen W, Wong MW, Gonzalez C, Pople JA (2016) Gaussian 16, Revision A.03. Gaussian, Inc., Wallingford CT

24. Grimme S (2006) Semiempirical GGA-type density functional constructed with a long-range dispersion correction. J Comput Chem 27:1787–1799. https://doi.org/10.1002/jcc.20495
25. Hirao H, Kumar D, Que L, Shaik S (2006) Two-state reactivity in alkane hydroxylation by non-heme iron−oxo complexes. J Am Chem Soc 128:8590–8606. https://doi.org/10.1021/ja061609o
26. Bathelt CM, Zurek J, Mulholland AJ, Harvey JN (2005) Electronic structure of compound I in human isoforms of cytochrome P450 from QM/MM modeling. J Am Chem Soc 127:12900–12908. https://doi.org/10.1021/ja0520924
27. Siegbahn PEM, Borowski T (2006) Modeling enzymatic reactions involving transition metals. Acc Chem Res 39:729–738. https://doi.org/10.1021/ar050123u
28. Hay PJ, Wadt WR (1985) Ab initio effective core potentials for molecular calculations. Potentials for the transition metal atoms Sc to Hg. J Chem Phys 82:270–283. https://doi.org/10.1063/1.448799
29. Wadt WR, Hay PJ (1985) Ab initio effective core potentials for molecular calculations. Potentials for main group elements Na to Bi. J Chem Phys 82:284–298. https://doi.org/10.1063/1.448800
30. Hay PJ, Wadt WR (1985) Ab initio effective core potentials for molecular calculations. Potentials for K to Au including the outermost core orbitals. J Chem Phys 82:299–310. https://doi.org/10.1063/1.448975
31. Becke AD (1997) Density-functional thermochemistry. V. Systematic optimization of exchange-correlation functionals. J Chem Phys 107:8554–8560. https://doi.org/10.1063/1.475007
32. Hay PJ, ThomH D (1977) The electronic states of KrF. J Chem Phys 66:1306–1316. https://doi.org/10.1063/1.434025
33. Latypov SK, Polyancev FM, Yakhvarov DG, Sinyashin OG (2015) Quantum chemical calculations of ^{31}P NMR chemical shifts: scopes and limitations. Phys Chem Chem Phys 17:6976–6987. https://doi.org/10.1039/c5cp00240k
34. Jilal I, El Barkany S, Bahari Z et al (2018) Unconventional synthesis, characterization and theoretical study (HF and DFT computations) of new cellulosic copper complex: benzyloxyethyl cellulose copper (CuBEC). Cellulose 25:4375–4388. https://doi.org/10.1007/s10570-018-1909-x
35. Raftani M, Abram T, Azaid A et al (2021) Theoretical design of new organic compounds based on diketopyrrolopyrrole and phenyl for organic bulk heterojunction solar cell applications: DFT and TD-DFT study. Mater Today: Proc 45:7334–7343. https://doi.org/10.1016/j.matpr.2020.12.1228
36. Pople JA, Radom L, Hehre WJ (1971) Molecular orbital theory of the electronic structure of organic compounds. VII. Systematic study of energies, conformations, and bond interactions. J Am Chem Soc 93:289–300. https://doi.org/10.1021/ja00731a001
37. Dennington R, Keith TA, Millam JM (n.d.) GaussView 6.1.1 Release Notes | Gaussian.com, https://gaussian.com/gv611rn/〉
38. Allouche A-R (2010) Gabedit-A graphical user interface for computational chemistry softwares. J Comput Chem 32:174–182. https://doi.org/10.1002/jcc.21600
39. Cossi M, Barone V, Robb MA (1999) A direct procedure for the evaluation of solvent effects in MC-SCF calculations. J Chem Phys 111:5295–5302. https://doi.org/10.1063/1.479788
40. Cossi M, Rega N, Scalmani G, Barone V (2001) Polarizable dielectric model of solvation with inclusion of charge penetration effects. J Chem Phys 114:5691–5701. https://doi.org/10.1063/1.1354187
41. Schäfer A, Horn H, Ahlrichs R (1992) Fully optimized contracted Gaussian basis sets for atoms Li to Kr. J Chem Phys 97:2571–2577. https://doi.org/10.1063/1.463096
42. Schäfer A, Huber C, Ahlrichs R (1994) Fully optimized contracted Gaussian basis sets of triple zeta valence quality for atoms Li to Kr. J Chem Phys 100:5829–5835. https://doi.org/10.1063/1.467146
43. Sakr MAS, Sherbiny FF, El-Etrawy A-A (2022) Hydrazone-based materials; DFT, TD-DFT, NBO analysis, Fukui function, MESP analysis, and solar cell applications. J Fluoresc 32:1857–1871. https://doi.org/10.1007/s10895-022-03000-6
44. Weigend F, Ahlrichs R (2005) Balanced basis sets of split valence, triple zeta valence and quadruple zeta valence quality for H to Rn: Design and assessment of accuracy. Phys Chem Chem Phys 7:3297. https://doi.org/10.1039/b508541a
45. Neese F (2017) Software update: the ORCA program system, version 4.0. Wires Comput Mol Sci 8:e1327. https://doi.org/10.1002/wcms.1327
46. Tenderholt, Adam L (n.d.) "QMForge: A program to analyze quantum chemistry calculations", Version 3.2, https://qmforge.net
47. Bolli A, Marino M, Rimbach G et al (2010) Flavonoid binding to human serum albumin. Biochem Biophys Res Commun 398:444–449. https://doi.org/10.1016/j.bbrc.2010.06.096
48. Sadr MH, Soltani B, Jalili A et al (2012) Synthesis and characterization of copper(II) complexes incorporating pyrazolyl-derived N, S-donor bidentate ligands. Transit Met Chem 37:611–617. https://doi.org/10.1007/s11243-012-9629-9
49. Matsia S, Tsave O, Hatzidimitriou A, Salifoglou A (2022) Chromium flavonoid complexation in an antioxidant capacity role. Int J Mol Sci 23:7171. https://doi.org/10.3390/ijms23137171
50. Selvaraj S, Krishnaswamy S, Devashya V et al (2013) Flavonoid-metal ion complexes: a novel class of therapeutic agents. Med Res Rev 34:677–702. https://doi.org/10.1002/med.21301
51. Tanui HK, Nkabyo HA, Pearce BH et al (2022) Iron(III) and copper(II) complexes derived from the flavonoids morin and quercetin: Chelation, crystal structure and DFT studies. J Mol Struct 1257:132591. https://doi.org/10.1016/j.molstruc.2022.132591
52. Kumar M, Gupta MK, Rizvi MA, Ansari A (2023) Electronic structures and ligand effect on redox potential of iron and cobalt complexes: a computational insight. Struct Chem 34:1565–1575. https://doi.org/10.1007/s11224-022-02119-3
53. Khajehzadeh M, Sadeghi N (2018) Molecular structure, X-ray crystallography, spectroscopic characterization, solvent effect, NLO, NBO, FMO analysis of [Cu(bpabza)] complexe. J Mol Liq 249:281–293. https://doi.org/10.1016/j.molliq.2017.10.142
54. Bhalla P, Tomer N, Goel A et al (2022) Chemoselective detection based on experimental and theoretical calculations of Cu^{2+} ions via deprotonation of chromone derived probe and its application. J Mol Struct 1264:133251–133251. https://doi.org/10.1016/j.molstruc.2022.133251
55. Moghim MT, Jamehbozorgi S, Rezvani M, Ramezani M (2022) Computational investigation on the geometry and electronic structures and absorption spectra of metal-porphyrin-oligo- phenyleneethynylenes-[60] fullerene triads. Spectrochim Acta A Mol Biomol Spectrosc 280:121488–121488. https://doi.org/10.1016/j.saa.2022.121488
56. Kumar M, Ansari M, Ansari A (2023) Electronic, geometrical and photophysical facets of five coordinated porphyrin N-heterocyclic carbene transition metals complexes: A theoretical study. Spectrochim Acta A Mol Biomol Spectrosc 284:121774–121774. https://doi.org/10.1016/j.saa.2022.121774

57. Geerlings P, De Proft F, Langenaeker W (2003) Conceptual density functional theory. Chem Rev 103:1793–1874. https://doi.org/10.1021/cr990029p
58. Govindarajan M, Karabacak M, Periandy S, Tanuja D (2012) Spectroscopic (FT-IR, FT-Raman, UV and NMR) investigation and NLO, HOMO–LUMO, NBO analysis of organic 2,4,5-trichloroaniline. Spectrochim Acta A Mol Biomol Spectrosc 97:231–245. https://doi.org/10.1016/j.saa.2012.06.014
59. Zumdahl SS, Zumdahl SA (2000) Chemistry for chemical and biological sciences, 5th ed. Houghton Mifflin 1–1234. https://www.biblio.com/9780395985816
60. Ghahramanpour M, Jamehbozorgi S, Rezvani M (2020) The effect of encapsulation of lithium atom on supramolecular triad complexes performance in solar cell by using theoretical approach. Adsorption 26:471–489. https://doi.org/10.1007/s10450-019-00196-1
61. Jamehbozorgi S, Ghahramanpour M, Rezvani M (2022) The role of insertion of Li atom in C60-Porphyrin-Metalloporphyrin, M = (V, Cr, Ni, Cu) as dyes in the DSSC by using the theoretical outlook. Int J New Chem 9:102–128. https://doi.org/10.22034/ijnc.2022.1.8
62. Mohammadzaheri M, Saeed J, Rezvani M et al (2023) Toward functionalization of ZnO nanotube and monolayer with 5-aminolevulinic acid drug as possible nanocarrier for drug delivery: a DFT based molecular dynamic simulations. Phys Chem Chem Phys 25:21492–21508. https://doi.org/10.1039/d3cp01490h
63. Rezvani M, Ganji MD, Bozorghi SJ, Niazi A (2018) DFT/TD-semiempirical study on the structural and electronic properties and absorption spectra of supramolecular fullerene-porphyrine-metalloporphyrine triads based dye-sensitized solar cells. Spectrochim Acta A Mol Biomol Spectrosc 194:57–66. https://doi.org/10.1016/j.saa.2017.12.073
64. Fatima K, Pandith AH, Manzoor T, Qureashi A (2023) DFT Studies on a metal oxide@graphene-decorated D–π_1–π_2–A novel multi-Junction light-harvesting system for efficient dye-sensitized solar cell applications. ACS Omega 8:8865–8875. https://doi.org/10.1021/acsomega.3c00333
65. Malashi NM, Jande YAC, Wazzan N et al (2024) Designed complexes combining brazilein and brazilin with betanidin for dye-sensitized solar cell application: DFT and TD-DFT study. J Mol Graph Model 127:108691–108691. https://doi.org/10.1016/j.jmgm.2023.108691
66. Rasool F, Wu G, Shafiq I et al (2024) Heterocyclic donor moiety effect on optical nonlinearity behavior of chrysene-based chromophores with push–pull configuration *via* the quantum chemical approach. ACS Omega 9:3596–3608. https://doi.org/10.1021/acsomega.3c07596
67. Malhotra SS, Kumar M, Gupta MK, Ansari A (2024) Theoretical exploration of copper based electrolytes for third generation dye sensitized solar cells. Mater Today Commun 39:109208–109208. https://doi.org/10.1016/j.mtcomm.2024.109208
68. Mohapatra RK, Azam M, Mohapatra PK et al (2022) Computational studies on potential new anti-Covid-19 agents with a multi-target mode of action. J King Saud Univ Sci 34:102086–102086. https://doi.org/10.1016/j.jksus.2022.102086
69. Yadav O, Ansari M, Ansari A (2021) Electronic structures, bonding and energetics of non-heme mono and dinuclear iron-TPA complexes: a computational exploration. Struct Chem 32:2007–2018. https://doi.org/10.1007/s11224-021-01775-1
70. Reed AE, Curtiss LA, Weinhold F (1988) Intermolecular interactions from a natural bond orbital, donor-acceptor viewpoint. Chem Rev 88:899–926. https://doi.org/10.1021/cr00088a005
71. Weinhold F, Landis CR (2005) Valency and bonding: a natural bond and orbital donor-acceptor perspective. Cambridge Univ. Press, Cambridge 1–749. https://doi.org/10.1017/CBO9780511614569
72. Ansari A, Ansari M, Singha A, Rajaraman G (2017) Interplay of electronic cooperativity and exchange coupling in regulating the reactivity of diiron(IV)-oxo complexes towards C−H and O−H Bond activation. Eur J Chem 23:10110–10125. https://doi.org/10.1002/chem.201701059
73. Kumar M, Talakkal AK, Mohapatra RK, Ansari A (2023) Photophysical properties of four-membered BN3 heterocyclic compounds: theoretical insights. J Mol Model 29:336. https://doi.org/10.1007/s00894-023-05731-0
74. Azam M, Sahoo PK, Mohapatra RK et al (2022) Structural investigations, Hirsfeld surface analyses, and molecular docking studies of a phenoxo-bridged binuclear Zinc(II) complex. J Mol Struct 1251:132039–132039. https://doi.org/10.1016/j.molstruc.2021.132039
75. Yadav O, Kumar M, Mittal H et al (2022) Theoretical exploration on structures, bonding aspects and molecular docking of α-aminophosphonate ligated copper complexes against SARS-CoV-2 proteases. Front Pharmacol 13:982484–982484. https://doi.org/10.3389/fphar.2022.982484
76. Sharma MK, Soumen S, Mahawar P et al (2019) Donor–acceptor-stabilised germanium analogues of acid chloride, ester, and acyl pyrrole compounds: synthesis and reactivity. Chem Sci 10:4402–4411. https://doi.org/10.1039/c8sc05380d
77. Yadav S, Kumar R, Vipin Raj K et al (2020) Amidinato Germylene-Zinc Complexes: Synthesis, Bonding, and Reactivity. Asian J Chem 19:3116–3121. https://doi.org/10.1002/asia.202000807
78. Yadav O, Ansari M, Ansari A (2022) Electronic structures, bonding aspects and spectroscopic parameters of homo/hetero valent bridged dinuclear transition metal complexes. Spectrochim Acta A Mol Biomol Spectrosc 278:121331–121331. https://doi.org/10.1016/j.saa.2022.121331
79. Ahmad M, Khalid M, Khan MS et al (2020) Exploring catecholase activity in dinuclear Mn(II) and Cu(II) complexes: an experimental and theoretical approach. New J Chem 44:7998–8009. https://doi.org/10.1039/d0nj00605j
80. Shahid M, Mantasha I, Khan S et al (2021) Elucidating the contribution of solvent on the catecholase activity in a mononuclear Cu(II) system: An experimental and theoretical approach. J Mol Struct 1244:130878–130878. https://doi.org/10.1016/j.molstruc.2021.130878
81. Ahmed M, Gupta M, Ansari A (2023) DFT and TDDFT exploration on the role of pyridyl ligands with copper toward bonding aspects and light harvesting. J Mol Model 29:358. https://doi.org/10.1007/s00894-023-05765-4
82. Ahmed M, Malhotra SS, Yadav O et al (2024) DFT and TDDFT exploration on electronic transitions and bonding aspect of DPA and PTDC ligated transition metal complexes. J Mol Model 30:122. https://doi.org/10.1007/s00894-024-05912-5